

Article

Electrocatalytic Hydrodechlorination Using Supported Atomically Precise Gold Nanoclusters under Flow-Through Configuration

Zhiyuan Zhao ¹, Haochen Yan ², Fuqiang Liu ², Jie Yao ¹, Shijie You ^{1,*} and Yanbiao Liu ^{2,3,*} 

¹ State Key Laboratory of Urban Water Resource and Environment, School of Environment, Harbin Institute of Technology, Harbin 150090, China; 19bg29093@stu.hit.edu.cn (Z.Z.); yaojie@hit.edu.cn (J.Y.)

² College of Environmental Science and Engineering, Donghua University, Shanghai 201620, China; 2212135@mail.dhu.edu.cn (H.Y.); liufuqiang@stu.ecnu.edu.cn (F.L.)

³ Shanghai Institute of Pollution Control and Ecological Security, 1239 Siping Road, Shanghai 200092, China

* Correspondence: sjyou@hit.edu.cn (S.Y.); yanbiaoliu@dhu.edu.cn (Y.L.); Tel.: +86-21-67798752 (Y.L.)

Abstract: We developed and optimized an electrocatalytic filtration system to catalytically hydrodechlorinate chlorophenolic compounds. A key part of the system was the cathode, which consisted of a filter constructed with electroactive carbon nanotubes (CNTs) functionalized with atomically precise gold nanoclusters (AuNCs). In the functional membrane electrode, the AuNCs attached to the CNTs functioned as a highly effective hydrodechlorination catalyst. Additionally, the ligands of the AuNCs facilitated the binding of the AuNCs with the CNT and protected the Au core from agglomeration. Atomic H^{*} was the primary reactive species in the system, but direct reduction by cathode electrons also contributed to the elimination of 2,4-dichlorophenol (2,4-DCP) by hydrodechlorination. The generated atomic H^{*} was able to break the C–Cl bond to achieve the rapid hydrodechlorination of 2,4-DCP into phenol, with 91.5% 2,4-DCP removal within 120 min. The AuNC catalysts attached to the CNT exceeded the best catalytic activity of larger nanoparticles (e.g., AuNPs), while the flow-through construction performed better than a standard batch reactor due to the convection-enhanced mass transport. The study provides an environmentally friendly strategy for the elimination of pervasive halogenated organic contaminants using a highly efficient, stable and recyclable system for hydrodechlorination that integrates nanofiltration and electrochemistry.

Keywords: gold nanoclusters; carbon nanotubes; hydrodechlorination; 2,4-dichlorophenol; advanced reduction process



Citation: Zhao, Z.; Yan, H.; Liu, F.; Yao, J.; You, S.; Liu, Y. Electrocatalytic Hydrodechlorination Using Supported Atomically Precise Gold Nanoclusters under Flow-Through Configuration. *Catalysts* **2023**, *13*, 1045. <https://doi.org/10.3390/catal13071045>

Academic Editors: Justo Lobato and Luisa Maria Gomez-Sainero

Received: 3 June 2023

Revised: 16 June 2023

Accepted: 26 June 2023

Published: 28 June 2023



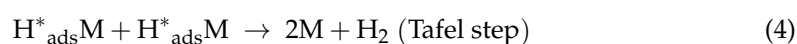
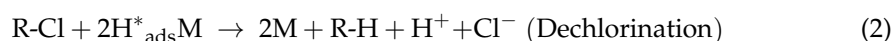
Copyright: © 2023 by the authors. Licensee MDPI, Basel, Switzerland. This article is an open access article distributed under the terms and conditions of the Creative Commons Attribution (CC BY) license (<https://creativecommons.org/licenses/by/4.0/>).

1. Introduction

Chlorophenolic organic compounds are widely used as raw materials or intermediates in the industrial production of pesticides, textile, dyes and petrochemicals [1]. However, due to the existence of chlorine atoms, the degradation cycle of chlorophenolic organic compounds is extremely long, which leads to their ubiquitous persistence in water systems and straightforward enrichment in aquatic organisms [2]. As a representative chlorophenolic organic chemical, 2,4-dichlorophenol (2,4-DCP) is known for being difficult to treat with common mineralization techniques [3,4]. The Chinese government and the United States Environmental Protection Agency have already listed it as a priority pollutant [5,6]. Additionally, the World Health Organization has classified 2,4-DCP as a carcinogenic compound [7]. Therefore, there is an urgent need for the development of effective strategies to decontaminate water containing 2,4-DCP.

Although advanced oxidation processes are highly effective in the degradation of halogenated organic compounds, they might generate oxidation products with greater toxicity than the parent compound [8–10]. Alternatively, advanced reduction processes (ARPs) have shown great potential for the removal of chlorophenol pollutants by degrading

the target pollutant into simple by-products, rather than generating intermediates with higher toxicity [9,11]. Among ARPs, electrocatalytic hydrodechlorination has attracted much attention regarding chlorophenol degradation because of its convenient operation and mild reaction conditions [6,12]. Specifically, a metal catalyst can adsorb protons to generate highly reductive forms of hydrogen at a low overpotential and adsorb them onto the catalyst (H^*_{ads}), thus enabling an indirect pathway controlled by H^*_{ads} for the hydrodechlorination of chlorophenols [13]. Additionally, direct electron transfer between the pollutants and the functional electrode surface can also contribute to chemical reduction [14]. The formation of atomic H^* in the electrocatalytic hydrodechlorination process is shown in the chemical reactions below (M represents metal catalysts) [15]:



The formation of hydrogen (generated by the Heyrovsky and Tafel steps) is the main limiting step that inhibits the electrocatalytic hydrodechlorination efficiency [16,17]. To strengthen the hydrodechlorination process, noble metal catalysts such as Pd [18] and Au [19] have been used to modify the cathode. Compared with extensive studies on the H^* generation using Pd, however, only limited efforts have been devoted to the application of Au toward H^* production, since Au has been considered to be catalytically inert for a long time [20,21].

The Au catalytic activity is closely correlated to its particle size and a general trend is that the activity of Au catalysts increases with the decrease in Au size. For instance, Xu et al. [22] synthesized a series of nanocrystalline biphasic Pd–Au nanoparticles. These alloy catalysts showed significant activity and stability toward low-temperature CO oxidation, even at 300 K. Further decreasing the Au size to less than 2 nm, known as gold nanoclusters (AuNCs), one can observe highly contrasting and unique physicochemical behavior compared with AuNPs (with particle size >2 nm) [23,24]. AuNCs typically consist of several to a few hundred gold atoms and specific ligands, which guarantee their stability in solution [25]. Thanks to the size effect, nanoclusters can provide many more exposed active sites than nanoparticles and therefore offer great potential in accelerating the catalytic reaction kinetics. For example, Liu et al. [26] previously designed a flow-through electro-Fenton system based on a carbon nanotube (CNT) filter functionalized with atomically precise AuNCs, which outperformed their AuNP counterparts in terms of the electro-Fenton reaction.

Although several Au nanocatalysts have been developed recently for ARPs, the necessity for the post-separation of the used catalyst from the solution and their sluggish reaction kinetics have significantly limited their wide application [27,28]. This post-separation limitation can be resolved by integrating the Au nanocatalyst with optimized supporting materials to achieve easy recovery and reuse [29]. The support design avoids particle aggregation and exposes numerous active sites [30]. In terms of reaction kinetics, the flow-through configuration usually outperforms conventional batch systems due to the convection-enhanced mass transport, while conventional batch reactors are typically diffusion-limited [26,31].

Herein, we developed an effective electrocatalytic flow-through system based on atomically precise AuNCs for highly efficient hydrodechlorination. Highly conductive CNTs served as an excellent framework to host these ultras-small AuNC catalysts, which attached to the CNTs via hydrogen bonding and/or hydrophobic interactions to form AuNC@CNT hybrids. The one-dimensional CNTs easily formed three-dimensional CNT networks by vacuum filtration to support a flow-through operation and electrochemistry

involvement. Enhanced chlorophenol degradation kinetics were achieved because of the combined effects of the ultrasmall AuNCs and their numerous catalytic sites, the electrochemical enhancement of the reaction and the flow-through design. The effects of four process parameters on the catalytic performance were identified and optimized. The atomic H^{*} activation and hydrodechlorination mechanism was investigated by combining experimental results and theoretical calculations. This study offers insights into the design of stable and efficient flow-through electrocatalytic systems for the treatment of polluted water.

2. Results

2.1. Electrochemical 2,4-Dichlorophenol Hydrodechlorination

The morphology of the as-synthesized AuNC@CNT nanohybrid filters is available in our previous report, as well as in the Supplementary Materials (Figures S1–S6) [12,26]. The electrocatalytic hydrodechlorination of 2,4-DCP was performed in an AuNC@CNT filtration system; the removal efficiency of 2,4-DCP reached up to 91.5% by exerting a negative potential on the functional filter electrode under acidic conditions (Figure 1). In comparison, control experiments using a pristine CNT filter electrode exhibited negligible 2,4-DCP removal under the same conditions, thereby emphasizing the indispensable role played by the atomically precise AuNCs in the proposed technology. The AuNCs in this study contained several to a few hundred Au atoms and were stabilized in solution by ligands or organic components such as proteins and thiolates. The nanoscale size of the AuNCs magnified the catalytic activity of the Au by exposing more active sites. Such efficacy was comparable to or even higher than that of several state-of-the-art Pd-based catalytic systems (Table 1).

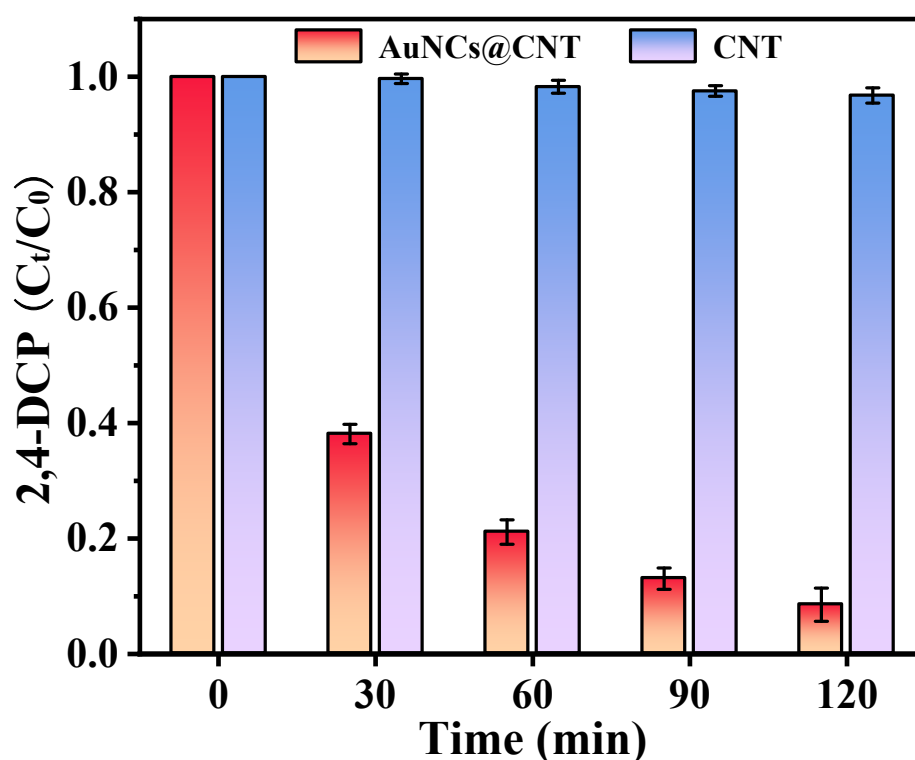


Figure 1. Comparison of electrocatalytic hydrodechlorination of 2,4-DCP using CNT and AuNC@CNT nanohybrid filters. Experimental conditions: applied potential = -1 V vs. Ag/Ag/Cl, $[2,4\text{-DCP}]_0 = 0.5$ mM, flow rate = 2.0 mL \cdot min $^{-1}$ and $\text{pH}_0 = 3.0$.

Table 1. Comparison of the 2,4-DCP hydrodechlorination performance of proposed system with reported systems.

Materials	External Energy	Pollutant Concentration	pH	Removal Efficiency	Ref.
Pd-MBfR	H ₂	0.1 mM		75% (2 h)	[32]
Pd/C	Electricity	0.31 mM	4.0	35.7% (2 h)	[33]
Pd/TiN	Electricity	0.31 mM	4.0	60.3% (2 h)	[33]
C-Pd	Electricity	0.31 mM	6.5	47.5% (2 h)	[34]
Pd/TiN	Electricity	0.31 mM	3.5	76.4% (2 h)	[35]
Pd-NiMOF/Ni foam	Electricity	0.045 mM	4.0	82.8% (2 h)	[36]
AuNC@CNT	Electricity	0.5 mM	3.0	91.5% (2 h)	This work

2.2. H^{*}-Mediated Electrocatalytic Hydrodechlorination Mechanism

We preliminarily inferred that two pathways could be responsible for the electrochemical hydrodechlorination process: (i) direct reduction by electron transfer between 2,4-DCP and the AuNC@CNT nanohybrid filter; and (ii) indirect reduction by atomic H^{*} produced during the electrolysis of water. CV was employed to elucidate the underlying mechanism. The AuNC@CNT nanohybrid filter electrode was first activated by continuous CV cycling between -1.5 and -0.5 V (vs. Ag/AgCl) at a sweep rate of 5 mV s^{-1} in N₂-saturated 50 mM Na₂SO₄ until a stable voltammogram diagram was obtained. Three oxidative peaks were detected in the CV measurements at different starting potentials (ranging from -1.5 to -0.5 V vs. Ag/AgCl) within the ranges of -1.0 to -0.8 , -0.3 to -0.1 and -0.1 to 0 V (vs. Ag/AgCl), as shown in Figure 2a. The three characteristic peaks can be associated with the oxidation of molecular H₂ at -0.80 V vs. Ag/AgCl, adsorbed H_{abs} (H^{*} adsorbed on the Au surface) at -0.30 to -0.10 V vs. Ag/AgCl and adsorbed H_{ads} (H^{*} adsorbed in the Au crystal lattice) at -0.10 to 0.00 V vs. Ag/AgCl [37]. These peak positions could shift depending on the practical operating conditions [38]. Additionally, the CV curves of the AuNC@CNT nanohybrid filter electrode with and without 2,4-DCP addition were compared to further clarify the role of H^{*}_{ads} and H^{*}_{abs} in the hydrodechlorination process. Figure 2b shows that the oxidative peak corresponding to H^{*}_{ads} was no longer present after the addition of 2,4-DCP, indicating that H^{*}_{ads} could serve as the primary active hydrogen species, rather than H₂ or H^{*}_{abs}. The mechanism of electrocatalytic hydrodechlorination was considered to be divided into direct electron transfer and indirect reduction via atomic H^{*}.

To further identify their contributions, quenching experiments were conducted using *t*-BuOH as a H^{*} scavenger. Figure 2c shows that the hydrodechlorination efficiency decreased from 91.5% to 70.3% when the concentration of the spiked *t*-BuOH increased from 0 to 100 mM, suggesting that atomic H^{*} contributed to the hydrodechlorination process. Noticeably, the degradation rate of 2,4-DCP with 100 mM *t*-BuOH could still reach 70.3% over a 120 min reaction, suggesting that direct electron transfer also played an essential role during 2,4-DCP hydrodechlorination. In addition, the contribution of atomic H^{*} and direct electron transfer to 2,4-DCP hydrodechlorination could be distinguished according to the scavenging test [39]. The removal of 2,4-DCP declined from 91.5% to 70.3% once H^{*} was quenched, suggesting that these two parts contributed 23.2% and 76.8% toward 2,4-DCP hydrodechlorination, respectively. EPR with DMPO as the spin trapping agent was used to confirm the active species responsible for the hydrodechlorination. As shown in Figure 2d, the reactive species were detected. No characteristic peak was observed for AuNC@CNT in the absence of an electric field. Nine of the main characteristic peaks associated with the DMPO-H^{*} adduct were detected in the AuNC@CNT system in the presence of an electric field, demonstrating the involvement of atomic H^{*} [40]. The addition of 2,4-DCP led to the formation of the DMPO-•OH adduct and the corresponding signals of DMPO-H^{*} disappeared consequently. To examine whether •OH contributed to 2,4-DCP, we further quenched H^{*} by purging O₂ in the solution (Figure S7). Results suggested that the 2,4-DCP removal was not enhanced compared with that quenched by *t*-BuOH.

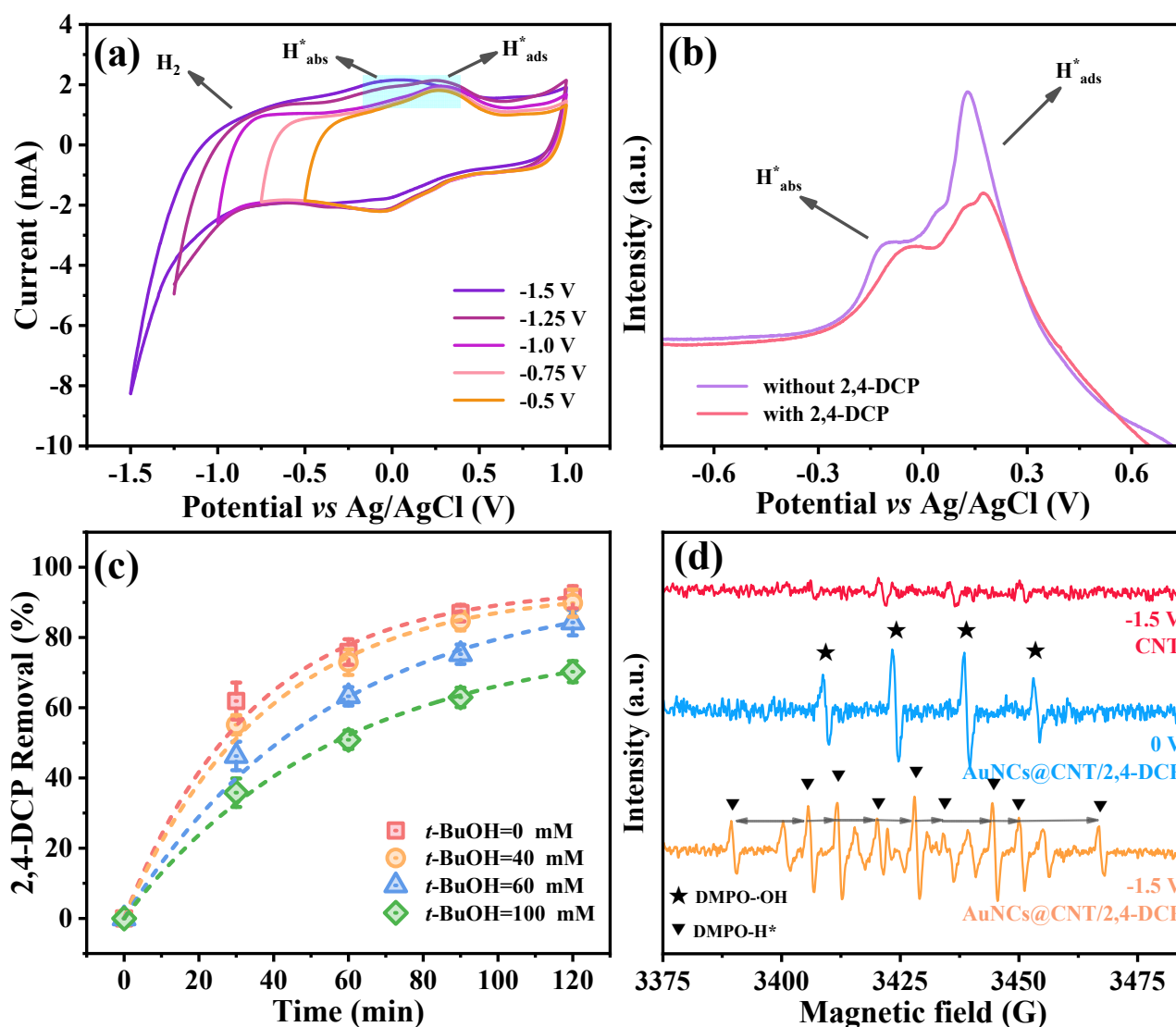
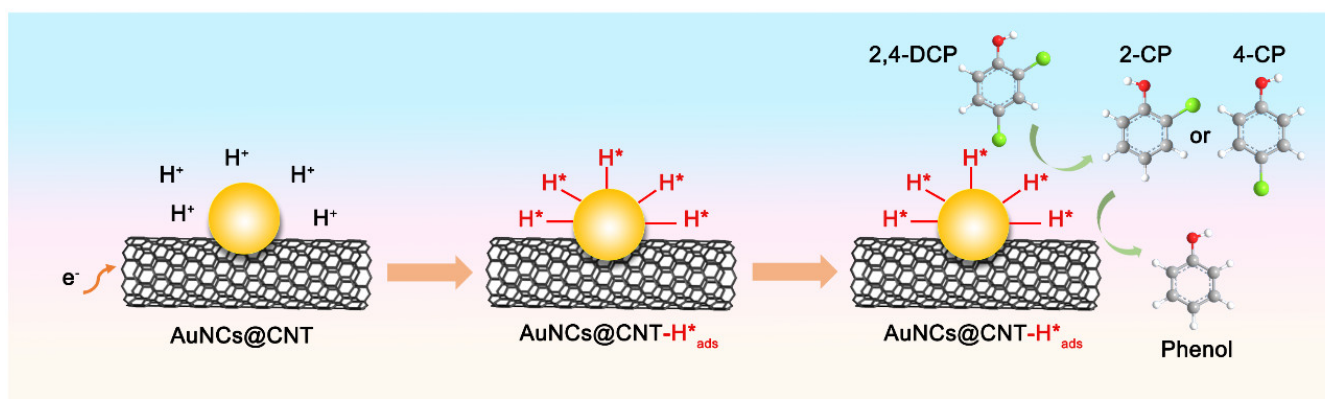


Figure 2. (a) CV curves of the AuNC@CNT nanohybrid filter with different starting potentials, from -1.5 to -0.5 V. The electrolyte contains 50 mM Na_2SO_4 . (b) CV curves of the AuNC@CNT nanohybrid filter with and without 2,4-DCP. The electrolyte contains 50 mM Na_2SO_4 and 0.5 mM 2,4-DCP. The CV scan rate was 5 mV/s. (c) The results of quenching with different t -BuOH concentrations. (d) The EPR spectra of CNT and AuNC@CNT nanohybrid filter in different systems using DMPO as the trapping agent during 2,4-DCP hydrodechlorination.

To obtain insights into the mechanism of 2,4-DCP hydrodechlorination, LC-MS was used to identify the electrolyzed intermediates (Figure S8). Several chlorophenol intermediates—for example, 2-CP, 4-CP ($m/z = 128.0$) and phenol ($m/z = 94.04$)—were identified in the AuNC@CNT system. Based on the LC-MS analysis, a 2,4-DCP hydrodechlorination pathway was developed (Scheme 1). The atomic H^* reacted with the ortho and para Cl atoms of 2,4-DCP to form 2- and 4-chlorophenol (2-CP and 4-CP, respectively). Notably, the 2-CP concentration stayed at a relatively high level throughout the process compared to the 4-CP concentration. The higher concentration of 2-CP was due to chemical reactions with lower Gibbs free energy (ΔG) and redox potential (E) [6]. The reaction that generated 2-CP had a lower E and ΔG than the reaction that produced 4-CP, while the opposite was true when 2- or 4-CP was the reactant. Finally, the fact that phenol was the primary final metabolite provided more information regarding the electrocatalytic hydrodechlorination process.

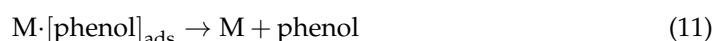
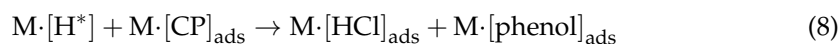
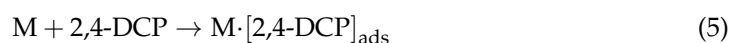


Scheme 1. Schematic illustration of the hydrodechlorination mechanism of 2,4-DCP using the AuNC@CNT nanohybrid filter.

To summarize, a schematic of the proposed hydrodechlorination mechanism of 2,4-DCP by the AuNC@CNT nanohybrid filter is depicted in Scheme 1. In brief, the AuNCs functioned as chemically selective, high-yielding nanoscale electrocatalysts that boosted the formation of atomic H*. Among them, H*_{ads} mediated the hydrodechlorination process while H*_{abs} remained inactive.

2.3. Density Functional Theory (DFT) Calculations

Density functional theory (DFT) calculations were employed to gain further insights into the 2,4-DCP hydrodechlorination pathways of the AuNCs [41,42]. The fine structure and physicochemical attributes of AuNCs were provided in previous reports [20,26]. As shown in Figure 3a, 2,4-DCP ($E_{\text{ad}} -1.88$ eV) exhibited a more negative adsorption energy (E_{ad}) on the surfaces of AuNCs compared to the atomic H* ($E_{\text{ad}} -1.35$ eV). This indicated a stronger interaction between 2,4-DCP and the Au sites, which would be beneficial for a subsequent hydrodechlorination process. Figure 3b displays the proposed 2,4-DCP hydrodechlorination routes on the surfaces of AuNCs based on the ΔG diagram. The electrocatalytic hydrodechlorination mechanism of 2,4-DCP can be expressed by Equations (5)–(11) (M represents the catalyst) [21]:



The key step in 2,4-DCP hydrodechlorination was the reaction from 2,4-DCP to 2-CP/4-CP, which needed to overcome a 1.36 eV activation energy barrier. In addition, the secondary hydrodechlorination exhibited a relatively lower energy barrier for the first step. Therefore, the subsequent reaction step was an energy release process and served to enable complete conversion from 2-CP/4-CP to phenol.

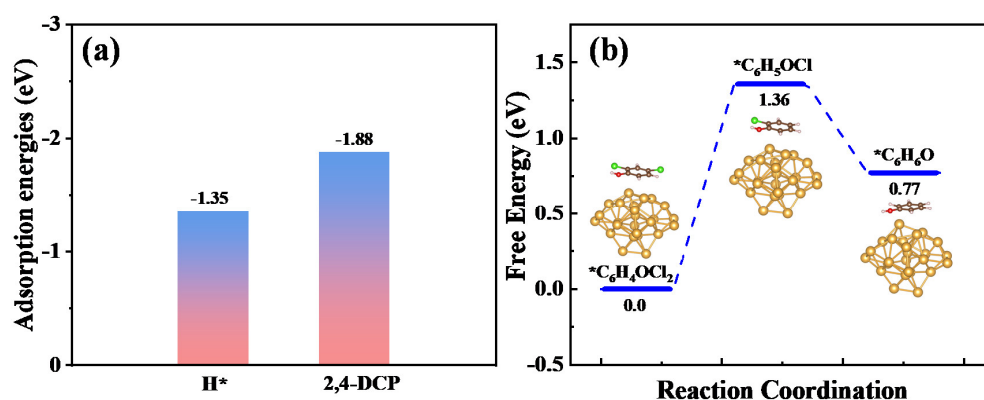


Figure 3. (a) Adsorption energies of atomic H (H^*) and 2,4-DCP on AuNC surface. (b) Free energy diagram of the hydrodechlorination (2,4-DCP) process on AuNCs. The insets are atomic structures.

2.4. System Optimization

We further optimized a number of important parameters that affected the performance of the AuNC@CNT filters. To determine the optimal AuNC loading, we fabricated and evaluated AuNC@CNT nanohybrid filters with different loadings of AuNCs. The results indicated that as the AuNC concentration increased from 0 to 2 mM, the degradation yield of 2,4-DCP increased from ~0% to 91.5% under similar conditions (Figure 4a). This was expected because the Au atoms of AuNCs were active centers and higher Au loading was conducive to more active sites. However, further increasing the AuNC loading to 3 mM resulted in a reduction in 2,4-DCP degradation due to the inevitable agglomeration of AuNCs at elevated concentrations.

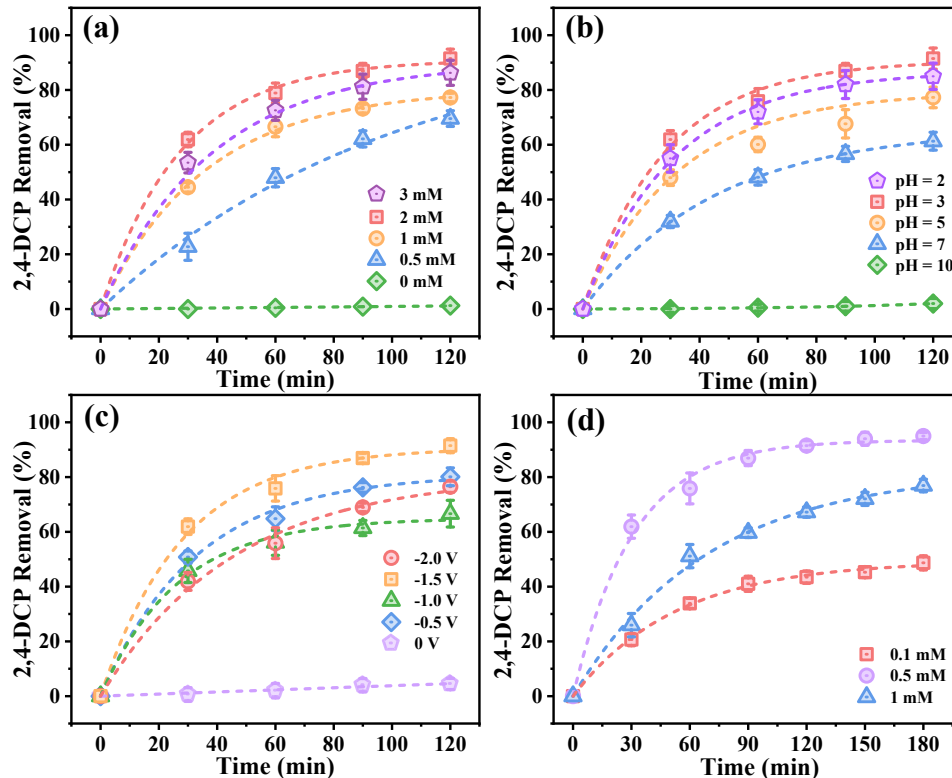


Figure 4. Optimization of the hydrodechlorination of 2,4-DCP parameters: (a) AuNC loading, (b) initial pH, (c) applied potential and (d) 2,4-DCP concentration.

The catholyte pH played a vital role in determining the hydrodechlorination performance by impacting the H^* yield, as illustrated in Equations (12)–(15) [6]:

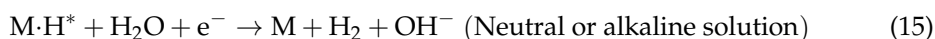
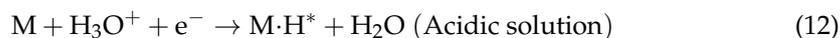


Figure 4b shows that the greatest degradation efficiency of 91.5% was achieved at a pH of 3.0. In contrast, a sharp decay in the efficiency was observed under neutral (pH 7, 38.7%) or alkaline (pH 10, ~0%) conditions. The alkaline condition could inhibit the dominant yield of atomic H^* , while the competing effect of the hydrogen evolution reaction could not be ignored in strongly acidic conditions (e.g., pH = 2). We also determined the dissolubility of 2,4-DCP as a function of the solution pH and only a negligible difference was found. This indicated that the pH effect on the hydrodechlorination performance was mainly derived from the yield of atomic H^* .

The effect of the applied potential (0 to -2 V) on the 2,4-DCP hydrodechlorination efficiency using the AuNC@CNT filters was characterized by comparing the AuNC@CNT results with results obtained using only CNT without AuNCs. Figure 4c shows that the 2,4-DCP degradation efficiency increased from 32.2% to 88.2% as the potential decreased from -0.5 V to -1.5 V (2 mM AuNC loading; pH 3; flow rate of $2 \text{ mL} \cdot \text{min}^{-1}$). However, a sharp drop in hydrodechlorination occurred when the applied potential was decreased to -2 V, possibly due to the increase in other reactions that competed with the electrocatalytic hydrodechlorination process (e.g., enhanced H_2 formation at low potential). Based on these results, an applied potential of -1.5 V was selected as the best one for subsequent investigations.

Moreover, the initial 2,4-DCP concentration affected the hydrodechlorination efficiency as well. The best hydrodechlorination performance was recorded at an initial concentration of 0.5 mM, as shown in Figure 4d. A further increase in the 2,4-DCP concentration (>0.5 mM) could lead to incomplete hydrodechlorination. This could be due to the mass transport limitations of the specific construction of the AuNC@CNT membrane system. Specifically, a high concentration could facilitate the diffusion of substrates to the electrode surface, while the hydrodechlorination efficiency could decrease due to the limited availability of active sites [43].

2.5. System Stability Evaluation

The durability of heterogeneous ARPs relies on robust catalysts designed for practical applications. In this regard, the robustness of the AuNC@CNT nanohybrid filter was evaluated by consecutive cycles of 2,4-DCP hydrodechlorination. The amount of 2,4-DCP eliminated by the filter decreased by only 5% over eight consecutive running cycles (Figure 5a), indicating that the nanohybrid filters had excellent stability. In addition, the leachable Au in the effluent was analyzed with ICP-MS. The outcomes of the analysis suggested that only negligible Au leakage was detected throughout the catalytic reaction. This could be attributed to the stable and large-surface-area networks constructed by the CNT. Moreover, the hydrophobic interactions and hydrogen bonding between the CNT sidewalls and hydrophobic ligands of AuNCs enabled the safe anchoring of the AuNCs onto the CNT networks, thereby preventing the AuNCs from aggregating and leaching into the substrate solution.

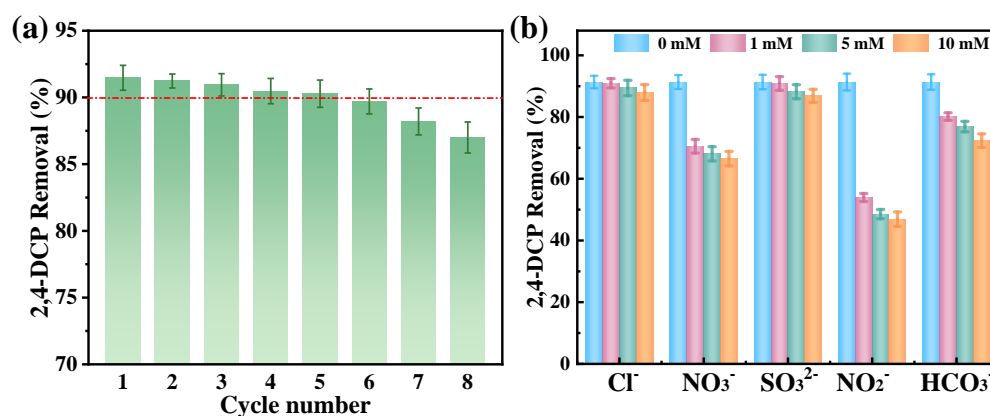
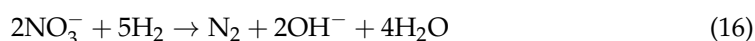


Figure 5. Evaluation of the hydrodegradation efficiency of 2,4-DCP over consecutive running cycles (a) and in the presence of different competitive anions (b). Experimental conditions: applied potential = -1 V vs. Ag/AgCl, $[2,4\text{-DCP}]_0 = 0.5$ mM, flow rate = 2.0 mL \cdot min $^{-1}$ and $\text{pH}_0 = 3.0$.

Analysis with FESEM revealed that the AuNC@CNT filters retained good morphologies after the operation (Figure S9). The surface chemistry of the AuNC@CNT nanohybrid filters was characterized in terms of their XPS spectra after the reaction. The XPS data confirmed that the O content decreased from 15.26 to 8.78 atom% for the fresh versus used catalyst, respectively. The change in the surface chemistry could be attributed to the electroreduction of the partially oxidized CNT and ligands of AuNCs by the excessive atomic H^* generated during the hydrodechlorination process. The Au valence state underwent a significant change, with the ratio of Au(I) to Au(0) increasing from 2.39 to 3.12 after the hydrodechlorination of 2,4-DCP (Figure S10). However, the overall Au content was constant, indicating that the Au species were preserved well. These results demonstrate that the AuNC@CNT nanohybrid filter was a robust electrocatalyst that could withstand multiple cycles of reaction without a significant loss of activity.

To explore the feasibility of using an electroactive hybrid filter for practical applications, we conducted a thorough investigation of the elimination of 2,4-DCP in the presence of competitive anions (e.g., Cl^- , SO_3^{2-} , NO_2^- , NO_3^- and HCO_3^-) with an initial concentration of 10 mM. The obtained results, as shown in Figure 5b, unraveled the effects of coexisting ions on the performance of hydrodechlorination by the AuNC@CNT nanohybrid filter. We observed that the addition of Cl^- and SO_3^{2-} had slight negative impacts on the 2,4-DCP removal efficiency (87.9% and 86.9%, respectively). The addition of HCO_3^- also suppressed the dichlorination kinetics and ultimately led to the 70.3% removal of 2,4-DCP. However, the introduction of NO_3^- resulted in a significant inhibitory effect on hydrodechlorination, leading to a decrease in the removal efficiency of 2,4-DCP to 66.5%. This was primarily due to NO_3^- competing for the available atomic H^* , leaving less H_2 available for the hydrodechlorination process (Equation (16)) [36]. In addition to NO_3^- , the introduction of NO_2^- also severely inhibited the hydrodechlorination process. NO_2^- possessed a significant inhibitory effect on hydrodechlorination, causing the removal yield of 2,4-DCP to decrease to 33.1%. This inhibition was most likely due to competition from NO_2^- reduction for both electrons and atomic H^* (Equation (17)) [44].



Overall, these findings demonstrate the critical importance of considering the effects of coexisting ions on the performance of electrocatalytic processes, particularly in the context of wastewater treatment. By gaining a deeper understanding of the underlying mechanisms at play, we can take steps to optimize these processes and pave the way for more efficient and effective wastewater treatment technologies.

3. Materials and Methods

3.1. Chemicals and Materials

All chemicals used were of analytical grade and used without further purification. Multiwalled carbon nanotubes (CNTs) were provided by TimesNano Co., Ltd. (Chengdu, China). Au(III) chloride trihydrate ($\text{HAuCl}_4 \cdot 3\text{H}_2\text{O}$, $\geq 49\%$), sodium borohydride (NaBH_4 , $\geq 98\%$) and 6-mercaptohexanoic acid (6-MHA, 90%) were purchased from Sigma-Aldrich (St. Louis, MO, USA). Sodium hydroxide (NaOH , $\geq 96\%$), N-methyl-2-pyrrolidinone (NMP, $\geq 99.5\%$), methanol (CH_3OH , $\geq 96\%$), ethanol ($\text{C}_2\text{H}_5\text{OH}$, $\geq 96\%$), hydrochloric acid (HCl , 36.0%~38.0%), sodium sulfate (Na_2SO_4 , $\geq 99\%$), sodium nitrate (NaNO_3 , $\geq 99\%$), sodium nitrite (NaNO_2 , $\geq 99\%$), sodium chloride (NaCl , $\geq 99\%$), sodium sulfide (Na_2S , $\geq 99\%$) and 2,4-dichlorophenol (2,4-DCP, $\text{C}_6\text{H}_4\text{Cl}_2\text{O}$, $\geq 99\%$) were obtained from Sinopharm Chemical Reagent Co., Ltd. (Shanghai, China). Ultrapure water produced from a Milli-Q Direct 8 purification system (Millipore, Billerica, MA, USA) was used for all experiments.

3.2. Preparation of AuNC@CNT Nanohybrid Filter

The CNT filter was fabricated by dispersing 30 mg of CNTs into 60 mL of NMP with probe ultrasonic treatment for 45 min; it was then loaded onto a PTFE membrane using vacuum filtration. The $\text{Au}_{25}(\text{MHA})_{18}$ NCs were synthesized using a NaOH-mediated NaBH_4^- reduction strategy [26]. The as-synthesized AuNCs were dialyzed at 0 °C for 3 h for further purification. The AuNC@CNT nanohybrid filters were prepared via a facile adsorption method. Briefly, 40 mL of AuNC solution was continuously passed through a CNT filter cathode for 90 min at a flow rate of $2 \text{ mL} \cdot \text{min}^{-1}$ and recirculated. The loaded AuNCs could be controlled by changing the concentration of the AuNCs from 0.25 to 1 mM.

3.3. Characterization

The morphology of the catalytic filters was characterized with a Hitachi S-4800 field emission scanning electron microscope (FESEM) and a JEM-2100F transmission electron microscope (TEM). A Thermo Fisher Scientific Escalab 250Xi X-ray photoelectron spectroscope (XPS) and Rigaku Smartlab X-ray diffractor (XRD) were utilized to examine the elemental compositions and crystal phases of the catalytic filters. The electrochemical activity of the catalytic filters was probed with cyclic voltammetry (CV) and electrochemical impedance spectroscopy (EIS) using a CHI 660E electrochemical workstation (CH Instrument, China) in a three-electrode configuration consisting of a AuNC@CNT working electrode, a Pt foil counter electrode and an Ag/AgCl reference electrode. CV analysis was performed at a scan rate of 5 mV/s in the 50 mM Na_2SO_4 solution. EIS analysis was performed over a frequency range of 10^5 to 10^{-2} Hz at an amplitude of 5 mV. A Thermo Scientific iCAP-Q inductively coupled plasma mass spectrometer (ICP-MS) was used to measure the Au concentration in the effluent. Electron paramagnetic resonance (EPR) spectra were obtained with a Bruker EMXnano EPR spectroscope (Germany) with 5,5-dimethyl-1-pyrroline N-oxide (DMPO) as a spin trapping agent. The 2,4-DCP hydrodechlorination products were determined by a liquid chromatography–mass spectrometry (LC-MS) system that combined an Agilent 6545 quadrupole time-of-flight mass spectrometry system with an Agilent 1290 Infinity II.

3.4. Electrochemical 2,4-Dichlorophenol Filtration Experiments

Electrochemical 2,4-DCP reduction experiments were run on commercial Whatman polycarbonate filtration casing with modifications for electrochemistry. A 10 mM 2,4-DCP stock solution in methanol was diluted with water to 0.5 mM. To avoid the effects of physical adsorption on the filtration of the 2,4-DCP, 100 mL of the 0.5 mM 2,4-DCP solution was first passed through the AuNC@CNT nanohybrid filter at $2.0 \text{ mL} \cdot \text{min}^{-1}$ for 1 h to achieve adsorption saturation. In a typical example of the recirculation mode of filtration, 2,4-DCP (0.5 mM) and a Na_2SO_4 (20 mM) electrolyte solution were passed through the AuNC@CNT nanohybrid filter and recirculated. The applied potential was determined with a CHI 660E electrochemical workstation in a three-electrode configuration. The impacts of the operational parameters (e.g., solution pH, AuNC loading and applied

filtration potential) on the catalytic performance were examined. The solution pH was controlled with 1 M NaOH or HCl. The system stability was evaluated with continuous 2,4-DCP filtration tests at a pH of 3 in recirculation mode. All electrocatalytic experiments were performed in triplicate to ensure reproducibility.

3.5. Analytical Methods

Effluent samples of 1 mL were taken at pre-determined intervals and immediately filtered through a 0.22 μm cellulose acetate membrane for further analysis. The concentration of 2,4-DCP was measured with high-performance liquid chromatography (HPLC, Shimadzu LC-20A, Japan). The parameters were set as follows: acetonitrile/water (0.1% phosphoric acid) (60:40, *v/v*) at room temperature. The injection volume was 10 μL and the UV detection wavelength was 220 nm. The flow rate of the mobile phase was 1 $\text{mL}\cdot\text{min}^{-1}$ with a Poroshell 120 EC- C_{18} column ($4.6 \times 100 \text{ mm}^2$, 2.7 μm). The conversion efficiency (%) was calculated as

$$\text{Conversion efficiency (\%)} = 100 \times (C_0 - C)/C_0 \quad (18)$$

where C_0 and C are the substrate concentrations before and after passing through the AuNC@CNT nanohybrid filter, respectively.

4. Conclusions

In this study, we designed a AuNC-based electrocatalytic nanohybrid filter through an electro-adsorption method. The hydrodechlorination of 2,4-DCP using the AuNC@CNT nanohybrid filter was systematically investigated. Experimental results revealed that H^* mediated the hydrodechlorination process and that cathode electrons can also reduce 2,4-DCP. DFT calculations and molecular characterizations clarified a two-step pathway for the hydrodechlorination of 2,4-DCP. The performance of the AuNC@CNT filter was enhanced by optimizing key factors such as the AuNC load, applied potential and initial pH. Additionally, the morphologically constrained structure of the CNT and the hydrophobic interactions and hydrogen bonding between the CNT sidewalls protected the active Au nanocatalysts from leaching into the solution, thus ensuring excellent sustainability and stability. Overall, the electrocatalytic filtration system based on AuNC@CNT provides a promising strategy for the effective elimination of persistent halogenated organic pollutants in groundwater.

Supplementary Materials: The following supporting information (Details on the theoretical calculations, LC-MS settings, characterization of the catalytic materials) can be downloaded at: <https://www.mdpi.com/article/10.3390/catal13071045/s1>. Text S1: DFT calculations; Text S2: LC-MS method; Text S3: Catalyst characterizations; Figure S1: FESEM image of (a) AuNC@CNT; (b) agglomerated AuNC@CNT; Figure S2: TEM images of AuNC@CNT; Figure S3: FESEM-EDS mapping images of AuNC@CNT; Figure S4: TGA curve of AuNC@CNT nanohybrid filter; Figure S5: (a) Comparison of the XPS survey spectrums of CNT and AuNC@CNT; (b) High resolution Au 4f XPS spectrum of AuNC@CNT; Figure S6: EIS spectra of the AuNC@CNT; Figure S7: Comparison of 2,4-DCP removal using different quenching agents; Figure S8: The MS spectra of (a) $m/z = 160.9600$, (b) $m/z = 126.9962$, (c) $m/z = 93.9603$; Figure S9: FESEM image of the AuNC@CNT after reaction; Figure S10: Comparison of the XPS survey spectrums of the Au 4f before and after reaction. Refs. [32–36,45–50] cited in Supplementary Materials.

Author Contributions: Z.Z.: data curation, methodology, writing—original draft; H.Y.: data curation, investigation, writing—original draft; F.L.: characterization; J.Y.: discussion; S.Y.: conceptualization, supervision; Y.L.: conceptualization, writing—review and editing, supervision. All authors have read and agreed to the published version of the manuscript.

Funding: This work was supported by the Open Project of State Key Laboratory of Urban Water Resource and Environment, Harbin Institute of Technology (No. QAK202108) and the National Natural Science Foundation of China (No. 52170068).

Data Availability Statement: All data supporting this study are available in the Supplementary Materials accompanying this paper.

Conflicts of Interest: The authors declare no conflict of interest.

References

1. Karci, A. Degradation of chlorophenols and alkylphenol ethoxylates, two representative textile chemicals, in water by advanced oxidation processes: The state of the art on transformation products and toxicity. *Chemosphere* **2014**, *99*, 1–18. [[CrossRef](#)] [[PubMed](#)]
2. Li, X.; Zhou, M.; Pan, Y.; Xu, L. Pre-magnetized Fe₀/persulfate for notably enhanced degradation and dechlorination of 2,4-dichlorophenol. *Chem. Eng. J.* **2017**, *307*, 1092–1104. [[CrossRef](#)]
3. Wu, P.; Yang, G.-P.; Zhao, X.-K. Sorption behavior of 2,4-dichlorophenol on marine sediment. *J. Colloid Interface Sci.* **2003**, *265*, 251–256. [[CrossRef](#)] [[PubMed](#)]
4. Pera-Titus, M.; García-Molina, V.; Baños, M.A.; Giménez, J.; Esplugas, S. Degradation of chlorophenols by means of advanced oxidation processes: A general review. *Appl. Catal. B* **2004**, *47*, 219–256. [[CrossRef](#)]
5. Sun, S.; Wang, Y.; Xu, C.; Qiao, C.; Chen, S.; Zhao, C.; Liu, Q.; Zhang, X. Reconstruction of microbiome and functionality accelerated crude oil biodegradation of 2,4-DCP-oil-contaminated soil systems using composite microbial agent B-Cl. *J. Hazard. Mater.* **2023**, *447*, 130808. [[CrossRef](#)]
6. Zhang, Z.; Cheng, R.; Nan, J.; Chen, X.; Huang, C.; Cao, D.; Bai, C.; Han, J.; Liang, B.; Li, Z.; et al. Effective electrocatalytic hydrodechlorination of 2,4,6-trichlorophenol by a novel Pd/MnO₂/Ni foam cathode. *Chin. Chem. Lett.* **2022**, *33*, 3823–3828. [[CrossRef](#)]
7. Elumalai, P.; Parthipan, P.; Huang, M.; Muthukumar, B.; Cheng, L.; Govarthanam, M.; Rajasekar, A. Enhanced biodegradation of hydrophobic organic pollutants by the bacterial consortium: Impact of enzymes and biosurfactants. *Environ. Pollut.* **2021**, *289*, 117956. [[CrossRef](#)]
8. Jiang, P.; Zhou, T.; Bai, J.; Zhang, Y.; Li, J.; Zhou, C.; Zhou, B. Nitrogen-containing wastewater fuel cells for total nitrogen removal and energy recovery based on Cl[•]/ClO[•] oxidation of ammonia nitrogen. *Water Res.* **2023**, *235*, 119914. [[CrossRef](#)]
9. Bouchoucha, H.; Bekkouche, S.; Merouani, S.; Dehane, A.; Hamdaoui, O. Solar chlorine activation for efficient Rhodamine B removal in strong basic pH: Processing conditions, radicals probing, and TiO₂ nanocatalyst effect. *Catalysts* **2023**, *13*, 942. [[CrossRef](#)]
10. Yang, L.; Jiao, Y.; Xu, X.; Pan, Y.; Su, C.; Duan, X.; Sun, H.; Liu, S.; Wang, S.; Shao, Z. Superstructures with atomic-level arranged perovskite and oxide layers for advanced oxidation with an enhanced non-free radical pathway. *ACS Sustain. Chem. Eng.* **2022**, *10*, 1899–1909. [[CrossRef](#)]
11. Sun, M.; Yan, F.; Zhang, R.; Reible, D.D.; Lowry, G.V.; Gregory, K.B. Redox control and hydrogen production in sediment caps using carbon cloth electrodes. *Environ. Sci. Technol.* **2010**, *44*, 8209–8215. [[CrossRef](#)] [[PubMed](#)]
12. Yan, H.; Liu, F.; Zhang, J.; Liu, Y. Facile synthesis and environmental applications of noble metal-based catalytic membrane reactors. *Catalysts* **2022**, *12*, 861. [[CrossRef](#)]
13. Weon, S.; Suh, M.; Chu, C.; Huang, D.; Stavitski, E.; Kim, J. Site-selective loading of single-atom Pt on TiO₂ for photocatalytic oxidation and reductive hydrodefluorination. *ACS EST Eng.* **2021**, *1*, 512–522. [[CrossRef](#)]
14. Ren, Y.; Zheng, W.; Li, S.; Liu, Y. Atomic H^{*}-mediated electrochemical removal of low concentration antimonite and recovery of antimony from water. *J. Hazard. Mater.* **2023**, *445*, 130520. [[CrossRef](#)]
15. Wu, Y.; Gan, L.; Zhang, S.; Song, H.; Lu, C.; Li, W.; Wang, Z.; Jiang, B.; Li, A. Carbon-nanotube-doped Pd-Ni bimetallic three-dimensional electrode for electrocatalytic hydrodechlorination of 4-chlorophenol: Enhanced activity and stability. *J. Hazard. Mater.* **2018**, *356*, 17–25. [[CrossRef](#)]
16. Eftekhari, A. Electrocatalysts for hydrogen evolution reaction. *Int. J. Hydrogen Energy* **2017**, *42*, 11053–11077. [[CrossRef](#)]
17. Li, Y.; Wang, H.; Xie, L.; Liang, Y.; Hong, G.; Dai, H. MoS₂ nanoparticles grown on graphene: An advanced catalyst for the hydrogen evolution reaction. *J. Am. Chem. Soc.* **2011**, *133*, 7296–7299. [[CrossRef](#)]
18. Wei, X.; Wan, X.; Miao, J.; Zhang, R.; Zhang, J.; Niu, Q.J. Hydrodechlorination of p-chlorophenol on Pd-coated Fe₃O₄@polypyrrole catalyst with ammonia borane as hydrogen donor. *Catal. Lett.* **2019**, *149*, 823–830. [[CrossRef](#)]
19. Mu, D.; Li, Z.; Yu, S.; Liu, S. Hydrodechlorination of chlorophenols with methanol as hydrogen donor over carbon nanotube supported Pd-catalysts. *Catal. Today* **2022**, *405–406*, 47–56. [[CrossRef](#)]
20. Yuan, X.; Zhang, B.; Luo, Z.; Yao, Q.; Leong, D.T.; Yan, N.; Xie, J. Balancing the rate of cluster growth and etching for gram-scale synthesis of thiolate-protected Au₂₅ nanoclusters with atomic precision. *Angew. Chem. Int. Ed.* **2014**, *53*, 4623–4627. [[CrossRef](#)] [[PubMed](#)]
21. Chen, Y.; Feng, C.; Wang, W.; Liu, Z.; Li, J.; Liu, C.; Pan, Y.; Liu, Y. Electronic structure engineering of bimetallic Pd-Au alloy nanocatalysts for improving electrocatalytic hydrodechlorination performance. *Sep. Purif. Technol.* **2022**, *289*, 120731. [[CrossRef](#)]
22. Xu, J.; White, T.; Li, P.; He, C.; Yu, J.; Yuan, W.; Han, Y.-F. Biphasic Pd-Au alloy catalyst for low-temperature CO oxidation. *J. Am. Chem. Soc.* **2010**, *132*, 10398–10406. [[CrossRef](#)] [[PubMed](#)]

23. Liu, X.; Li, Y.; Xing, Z.; Zhao, X.; Liu, N.; Chen, F. Monolithic carbon foam-supported Au nanoparticles with excellent catalytic performance in a fixed-bed system. *New J. Chem.* **2017**, *41*, 15027–15032. [[CrossRef](#)]
24. Yao, Q.; Chen, T.; Yuan, X.; Xie, J. Toward total synthesis of thiolate-protected metal nanoclusters. *Acc. Chem. Res.* **2018**, *51*, 1338–1348. [[CrossRef](#)] [[PubMed](#)]
25. Dharmaratne, A.C.; Krick, T.; Dass, A. Nanocluster size evolution studied by mass spectrometry in room temperature Au₂₅(SR)₁₈ synthesis. *J. Am. Chem. Soc.* **2009**, *131*, 13604–13605. [[CrossRef](#)]
26. Liu, F.; Liu, Y.; Yao, Q.; Wang, Y.; Fang, X.; Shen, C.; Li, F.; Huang, M.; Wang, Z.; Sand, W.; et al. Supported atomically-precise gold nanoclusters for enhanced flow-through electro-Fenton. *Environ. Sci. Technol.* **2020**, *54*, 5913–5921. [[CrossRef](#)]
27. Smirnov, E.; Peljo, P.; Scanlon, M.D.; Girault, H.H. Interfacial redox catalysis on gold nanofilms at soft interfaces. *ACS Nano* **2015**, *9*, 6565–6575. [[CrossRef](#)]
28. Priece, P.; Adekunle Salami, H.; Padilla, R.H.; Zhong, Z.; Lopez-Sanchez, J.A. Anisotropic gold nanoparticles: Preparation and applications in catalysis. *Chin. J. Catal.* **2016**, *37*, 1619–1650. [[CrossRef](#)]
29. Chen, Y.; Yan, B.; Cheng, Y. State-of-the-art review of oxidative dehydrogenation of ethane to ethylene over MoVNbTeO_x catalysts. *Catalysts* **2023**, *13*, 204. [[CrossRef](#)]
30. Lou, Z.; Yu, C.; Wen, X.; Xu, Y.; Yu, J.; Xu, X. Construction of Pd nanoparticles/two-dimensional Co-MOF nanosheets heterojunction for enhanced electrocatalytic hydrodechlorination. *Appl. Catal. B* **2022**, *317*, 121730. [[CrossRef](#)]
31. Kanafin, Y.N.; Abdirova, P.; Kanafina, D.; Arkhangelsky, E.; Kyzas, G.Z.; Pouloupos, S.G. UV and zero-valent iron (ZVI) activated continuous flow persulfate oxidation of municipal wastewater. *Catalysts* **2023**, *13*, 25. [[CrossRef](#)]
32. Wu, C.; Zhou, L.; Zhou, C.; Zhou, Y.; Zhou, J.; Xia, S.; Rittmann, B.E. A kinetic model for 2,4-dichlorophenol adsorption and hydrodechlorination over a palladized biofilm. *Water Res.* **2022**, *214*, 118201. [[CrossRef](#)] [[PubMed](#)]
33. Fu, W.; Wang, K.; Lv, X.; Fu, H.; Dong, X.; Chen, L.; Zhang, X.; Jiang, G. Palladium nanoparticles assembled on titanium nitride for enhanced electrochemical hydrodechlorination of 2,4-dichlorophenol in water. *Chin. J. Catal.* **2018**, *39*, 693–700. [[CrossRef](#)]
34. Jiang, G.; Lan, M.; Zhang, Z.; Lv, X.; Lou, Z.; Xu, X.; Dong, F.; Zhang, S. Identification of active hydrogen species on palladium nanoparticles for an enhanced electrocatalytic hydrodechlorination of 2,4-dichlorophenol in water. *Environ. Sci. Technol.* **2017**, *51*, 7599–7605. [[CrossRef](#)]
35. Jiang, G.S.; Li, J.; Shi, X.; Lv, X.; Huang, Y.-X.; Dong, F.; Jiang, G. Identifying the rate-determining step of the electrocatalytic hydrodechlorination reaction on palladium nanoparticles. *Nanoscale* **2019**, *11*, 15892–15899.
36. Shen, Y.; Tong, Y.; Xu, J.; Wang, S.; Wang, J.; Zeng, T.; He, Z.; Yang, W.; Song, S. Ni-based layered metal-organic frameworks with palladium for electrochemical dechlorination. *Appl. Catal. B* **2020**, *264*, 118505. [[CrossRef](#)]
37. Zheng, W.; You, S.; Yao, Y.; Jin, L.; Liu, Y. Development of atomic hydrogen-mediated electrocatalytic filtration system for peroxymonosulfate activation towards ultrafast degradation of emerging organic contaminants. *Appl. Catal. B* **2021**, *298*, 120593. [[CrossRef](#)]
38. Li, S.; Liu, C.; Lv, W.; Liu, G. Incorporating oxygen atoms in a SnS₂ atomic layer to simultaneously stabilize atomic hydrogen and accelerate the generation of hydroxyl radicals for water decontamination. *Environ. Sci. Technol.* **2022**, *56*, 4980–4987. [[CrossRef](#)]
39. Liu, F.; Wang, Z.; You, S.; Liu, Y. Electrogenerated quinone intermediates mediated peroxymonosulfate activation toward effective water decontamination and electrode antifouling. *Appl. Catal. B* **2023**, *320*, 121980. [[CrossRef](#)]
40. Zheng, W.; Liu, Y.; Liu, F.; Wang, Y.; Ren, N.; You, S. Atomic hydrogen in electrocatalytic systems: Generation, identification, and environmental applications. *Water Res.* **2022**, *223*, 118994. [[CrossRef](#)]
41. Li, Y.; Ma, J.; Wu, Z.; Wang, Z. Direct electron transfer coordinated by oxygen vacancies boosts selective nitrate reduction to N₂ on a Co-CuO_x electroactive filter. *Environ. Sci. Technol.* **2022**, *56*, 8673–8681. [[CrossRef](#)] [[PubMed](#)]
42. Wang, Y.; Zhou, W.; Jia, R.; Yu, Y.; Zhang, B. Unveiling the activity origin of a copper-based electrocatalyst for selective nitrate reduction to ammonia. *Angew. Chem. Int. Ed.* **2020**, *59*, 5350–5354. [[CrossRef](#)] [[PubMed](#)]
43. Mao, M.; Wu, J.; Wang, Y.; Long, Y.; Fan, G. Active site and adsorption behavior engineering of subsize PdNi nanoparticles for boosting electrocatalytic hydrodechlorination of 4-chlorophenol. *Appl. Surf. Sci.* **2022**, *600*, 153988. [[CrossRef](#)]
44. Wu, C.; Zhou, L.; Zhou, C.; Zhou, Y.; Xia, S.; Rittmann, B.E. Co-removal of 2,4-dichlorophenol and nitrate using a palladized biofilm: Denitrification-promoted microbial mineralization following catalytic dechlorination. *J. Hazard. Mater.* **2022**, *422*, 126916. [[CrossRef](#)] [[PubMed](#)]
45. Grimme, S.; Antony, J.; Ehrlich, S.; Krieg, H. A consistent and accurate ab initio parametrization of density functional dispersion correction (DFT-D) for the 94 elements H-Pu. *J. Chem. Phys.* **2010**, *132*, 154104. [[CrossRef](#)]
46. Kresse, G.; Joubert, D. From ultrasoft pseudopotentials to the projector augmented-wave method. *Phys. Rev. B* **1999**, *59*, 1758–1775. [[CrossRef](#)]
47. Perdew, J.P.; Burke, K.; Ernzerhof, M. Generalized gradient approximation made simple. *Phys. Rev. Lett.* **1996**, *77*, 3865–3868. [[CrossRef](#)]
48. Kresse, G.; Hafner, J. Ab initio molecular-dynamics simulation of the liquid-metal-amorphous-semiconductor transition in germanium. *Phys. Rev. B Condens Matter.* **1994**, *49*, 14251–14269. [[CrossRef](#)]

49. Kresse, G.; Hafner, J. Ab initio molecular dynamics for liquid metals. *Phys. Rev. B Condens Matter*. **1993**, *47*, 558–561. [[CrossRef](#)]
50. Liu, Y.; Zheng, Y.; Du, B.; Nasaruddin, R.R.; Chen, T.; Xie, J. Golden carbon nanotube membrane for continuous flow catalysis. *Ind. Eng. Chem. Res.* **2017**, *56*, 2999–3007. [[CrossRef](#)]

Disclaimer/Publisher's Note: The statements, opinions and data contained in all publications are solely those of the individual author(s) and contributor(s) and not of MDPI and/or the editor(s). MDPI and/or the editor(s) disclaim responsibility for any injury to people or property resulting from any ideas, methods, instructions or products referred to in the content.